

Revisiting Andromeda's Parachute[★]

Vyacheslav N. Shalyapin^{1,2,3}, Luis J. Goicoechea¹, Karianne Dyrland^{4,5}, and Håkon Dahle⁴

¹ Departamento de Física Moderna, Universidad de Cantabria, Avda. de Los Castros s/n, E-39005 Santander, Spain
e-mail: vshal@ukr.net; goicol@unican.es

² O.Ya. Usikov Institute for Radiophysics and Electronics, National Academy of Sciences of Ukraine, 12 Acad. Proskury St., UA-61085 Kharkiv, Ukraine

³ Institute of Astronomy of V.N. Karazin Kharkiv National University, Svobody Sq. 4, UA-61022 Kharkiv, Ukraine

⁴ Institute of Theoretical Astrophysics, University of Oslo, PO Box 1029, Blindern 0315, Oslo, Norway

⁵ Kongsberg Defence & Aerospace AS, Instituttveien 10, PO Box 26, 2027, Kjeller, Norway

September 15, 2023

ABSTRACT

The gravitational lens system PS J0147+4630 (Andromeda's Parachute) consists of four quasar images ABCD and a lensing galaxy. We obtained *r*-band light curves of ABCD in the 2017–2021 period from a monitoring with two 2-m class telescopes. These curves and state-of-the-art curve-shifting algorithms led to three independent time delays relative to image A, one of which is accurate enough (uncertainty of about 4%) to be used in cosmological studies. Our finely sampled light curves and some additional fluxes in the years 2010–2013 also demonstrated the presence of significant microlensing variations. This paper also focused on new near-IR spectra of ABCD in 2018–2019 that were derived from archive data of two 10-m class telescopes. We analysed the spectral region including the Mg II, H β , [O III], and H α emission lines (0.9–2.4 μ m), measuring image flux ratios and a reliable quasar redshift of 2.357 ± 0.002 , and finding evidence of an outflow in the H α emission. In addition, we updated the lens mass model of the system and estimated a quasar black-hole logarithmic mass $\log [M_{\text{BH}}/M_{\odot}] = 9.34 \pm 0.30$.

Key words. gravitational lensing: strong – quasars: individual: PS J0147+4630

1. Introduction

Optical frames from the Panoramic Survey Telescope and Rapid Response System (Pan-STARRS; Chambers et al. 2019) led to the serendipitous discovery of the strong gravitational lens system with a quadruply-imaged quasar (quad) PS J0147+4630 (Berghea et al. 2017). Due to its position in the sky and the spatial arrangement of the four quasar images, this quad is also called Andromeda's Parachute (e.g. Rubin et al. 2018). The three brightest images (A, B and C) forms an arc that is about 3'' from the faintest image D, and the main lens galaxy G is located between the bright arc and D. This configuration is clearly seen in the left panel of Figure 1, which is based on Hubble Space Telescope (HST) data.

As far as we know, the quasar PS J0147+4630 is the brightest source in the sky at redshifts $z > 1.4$ (apart from transient events such as gamma-ray bursts), and its four optical images can be easily resolved with a ground-based telescope in normal seeing conditions. Thus, it is a compelling target for various physical studies based on high-resolution spectroscopy (e.g. Rubin et al. 2018) and detailed photometric monitoring (e.g. Lee 2018). Early two-season monitoring campaigns with the 2.0 m Liverpool Telescope (LT; Goicoechea & Shalyapin 2019) and the 2.5 m Nordic Optical Telescope (NOT; Dyrland 2019) provided accurate optical light curves of all quasar images, as well as preliminary time delays and evidence of microlensing-induced variations. A deeper look at the optical variability of Andromeda's Parachute is of great importance, since robust time delays and

well-observed microlensing variations can be used to determine cosmological parameters (e.g. Treu & Marshall 2016) and the structure of the quasar accretion disc (e.g. Schmidt & Wambsganss 2010).

Early optical spectra of the system confirmed the gravitational lensing phenomenon and revealed the broad absorption-line (BAL) nature of the quasar (Lee 2017; Rubin et al. 2018). However, there is an appreciable discrepancy between the quasar redshift reported by Rubin et al. (2018) and that measured by Lee (2017), amounting to $\Delta z_s \sim 0.04$. Lee (2018) also performed the first attempt to determine the redshift of G from spectroscopic observations with the 8.1 m Gemini North Telescope (GNT). An accurate reanalysis of these GNT data showed that the first estimate of the lens redshift was biased, by enabling better identification of G as an early-type galaxy at $z_1 = 0.678 \pm 0.001$ with stellar velocity dispersion $\sigma_1 = 313 \pm 14 \text{ km s}^{-1}$ (Goicoechea & Shalyapin 2019). Both redshifts, z_s and z_1 , are key pieces of information to interpret, among other things, time delays and microlensing effects. Additionally, HST high-resolution imaging of the lens system provided a lens mass model (Shajib et al. 2019, 2021). To ensure proper interpretation of delays and microlensing-induced phenomena, a reliable lens mass model is also required.

New spectroscopic observations in the unexplored near-IR region are also useful tools to shed light on physical properties of the quad. In addition to the determination of redshifts, wavelength-domain data are often used to measure image flux ratios for emission lines and their underlying continua. These measurements provide insights about the macrolens flux ratios and extinction/microlensing effects (e.g. Motta et al. 2012; Goicoechea & Shalyapin 2016; Shalyapin & Goicoechea 2017).

[★] Tables 2, 4, 6, and 7 are only available in electronic form at the CDS via anonymous ftp to cdsarc.u-strasbg.fr (130.79.128.5) or via <http://cdsweb.u-strasbg.fr/cgi-bin/qcat?J/A+A/vol/page>

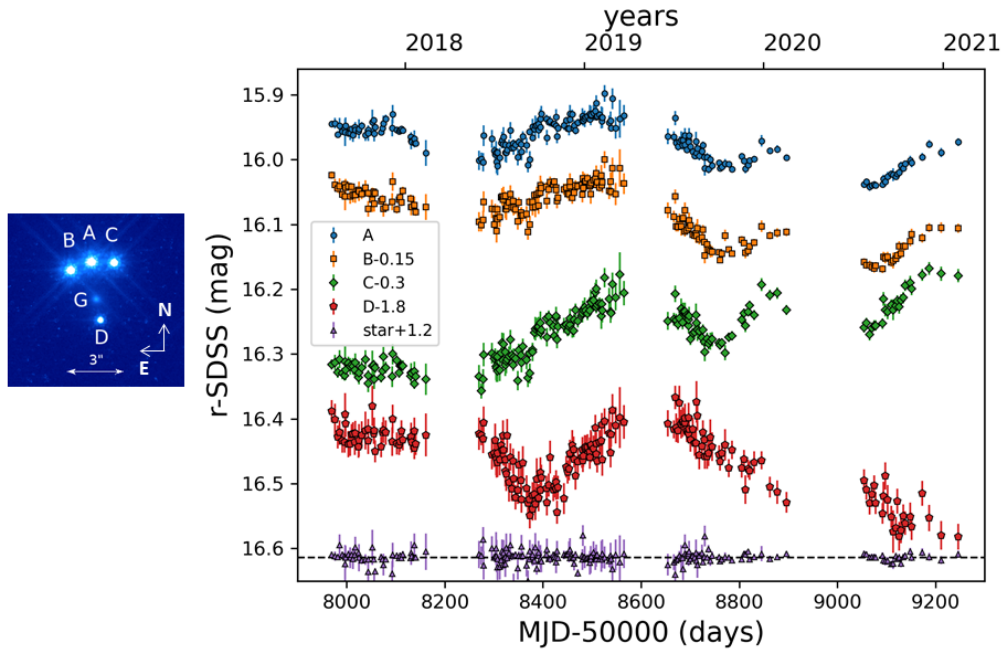


Fig. 1. *Left:* quasar images ABCD and main lens galaxy G of PS J0147+4630 from a public HST-WFC3 frame of the system in the F814W band. *Right:* LT-NOT light curves of PS J0147+4630 from its discovery to 2021. The r -band magnitudes of images B, C, and D, and the control star are offset by -0.15 , -0.3 , -1.8 , and $+1.2$, respectively, to facilitate comparison between them and with image A.

The macrolens flux ratios, for instance, put constraints on the distribution of mass lensing the quasar. Moreover, if one has information on the magnification and transmission factors for a given quasar image, line widths and continuum fluxes for such image yield estimates of the quasar black hole mass (e.g. Vestergaard & Peterson 2006; Assef et al. 2011), thus constraining the size of the innermost region in the accretion disc.

This paper is organized as follows. In Sect. 2, we present combined LT and NOT light curves of the four images of PS J0147+4630 spanning four observing seasons from 2017 to 2021. In Sect. 3, using these optical light curves, we carefully analyse the time delays between images and the quasar microlensing variability. In Sect. 4, we present an analysis of near-IR spectroscopic data of the system in 2018–2019, focusing on the quasar redshift and the image flux ratios. In Sect. 5, assuming a flat Λ CDM (standard) cosmology, we discuss the Hubble constant (H_0) value that is inferred from the lens mass model based on HST imaging, updated redshifts, and the longest time delay that we measure. A lens mass modelling based on astrometric and time-delay constraints is also discussed in Sect. 5. In Sect. 6, we measure the mass of the central black hole in the quasar. Our main conclusions are included in Sect. 7.

2. New optical light curves

We monitored PS J0147+4630 with the LT from 2017 August to 2021 February using the IO:O optical camera with a pixel scale of $\sim 0''.30$. Each observing night, a single 120 s exposure was taken in the Sloan r -band filter, and over the full monitoring period, 145 r -band frames were obtained. The LT data reduction pipeline carried out three basic tasks: bias subtraction, over-scan trimming, and flat fielding. Additionally, the IRAF soft-

ware¹ (Tody 1986, 1993) allowed us to remove cosmic rays and bad pixels from all frames. We extracted the brightness of the four quasar images ABCD through PSF fitting, using the IMFIT-FITS software (McLeod et al. 1998) and following the scheme described by Goicoechea & Shalyapin (2019). Table 1 includes the position and magnitudes of the PSF star, as well as of other relevant field stars. These data are taken from the Data Release 1 of Pan-STARRS² (Flewelling et al. 2020). Our photometric model consisted of four point-like sources (ABCD) and a de Vaucouleurs profile convolved with the empirical PSF (lensing galaxy G). Positions of components with respect to A and structure parameters of G were constrained from HST data (Shajib et al. 2019, 2021).

We also selected six non-variable blue stars in the field of PS J0147+4630 and performed PSF photometry on five of them (see the calibration stars Cal1–Cal5 in Table 1; Cal6 is a saturated star in LT frames). For each of the five calibration stars, we calculated its average magnitude within the monitoring period and magnitude deviations in individual frames (by subtracting average). In each individual frame, the five stellar magnitude deviations were averaged together to calculate a single magnitude offset, which was then subtracted from the magnitudes of quasar images. After this photometric calibration, we removed 15 observing epochs in which quasar magnitudes deviate appreciably from adjacent values. Thus, the final LT r -band light curves are based on 130 frames (epochs), and the typical uncertainties in the light curves of the quasar images and control star (see Table 1) were estimated from magnitude differences between adjacent epochs separated by no more than 4 d (Goicoechea & Shalyapin 2019).

¹ <https://iraf-community.github.io/>

² <http://panstarrs.stsci.edu>

Table 1. Pan-STARRS positions and magnitudes of relevant field stars.

Star	RA(J2000)	Dec(J2000)	<i>g</i>	<i>r</i>	<i>i</i>
PSF	26.773246	46.506670	16.366	15.606	15.260
Control	26.746290	46.504028	15.800	15.421	15.269
Cal1	26.805695	46.522834	16.587	16.292	16.208
Cal2	26.725610	46.488113	16.857	16.405	16.257
Cal3	26.752831	46.518659	17.157	16.836	16.718
Cal4	26.760809	46.474513	17.229	16.856	16.714
Cal5	26.824027	46.528718	15.656	15.200	15.029
Cal6	26.790480	46.502241	15.145	14.831	14.716

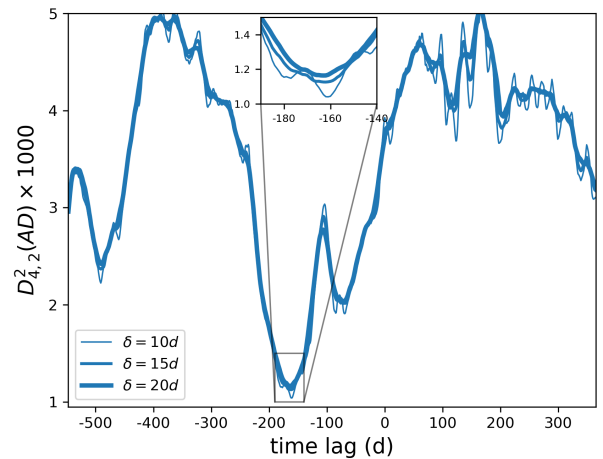
Notes. Astrometric and photometric data of the stars that we used for PSF fitting (PSF), variability checking (Control), and calibration (Cal1–Cal6). RA(J2000) and Dec(J2000) are given in degrees.

We derived typical errors of 0.0058 (A), 0.0069 (B), 0.0091 (C), 0.0188 (D), and 0.0054 (control star) mag. For the control star, we have also verified that its typical error practically coincides with the standard deviation of all measures (0.0051 mag). To obtain photometric uncertainties at each observing epoch, the typical errors were scaled by the relative signal-to-noise ratio of the PSF star (Howell 2006).

The optical monitoring of PS J0147+4630 with the NOT spanned from 2017 August to 2019 December. We used the AL-FOSC camera with a pixel scale of $\sim 0''.21$ and the *R*-Bessel filter. This passband is slightly redder than the Sloan *r* band. Each observing night, we mainly took three exposures of 30 s each under good seeing conditions. The full-width at half-maximum (FWHM) of the seeing disc was about $1''$, and we collected 298 individual frames over the entire monitoring campaign. After a standard data reduction, IMFITFITS PSF photometry yielded magnitudes for the quasar images (see above for details on the photometric model). To avoid biases in the combined LT-NOT light curves, the same photometric method was applied to LT and NOT frames. This method differs from that of Dyrland (2019), who used the DAOPHOT package in IRAF (Stetson 1987; Massey & Davis 1992) to extract magnitudes from NOT frames.

The six calibration stars in Table 1 were used to adequately correct quasar magnitudes (see above), and we were forced to remove 17 individual frames leading to magnitude outliers. We then combined *R*-band magnitudes measured on the same night to obtain photometric data of the lensed quasar and control star at 77 epochs. Again, typical errors were derived from magnitudes at adjacent epochs that are separated < 4.5 d. This procedure led to uncertainties of 0.0122 (A), 0.0122 (B), 0.0144 (C), 0.0197 (D), and 0.0170 (control star) mag. Errors at each observing epoch were calculated in the same way as for the LT light curves.

As a last step, we combined the *r*-band LT and *R*-band NOT light curves. If we focus on the quasar images and consider *rR* pairs separated by no more than 2.5 d, the values of the average colour $\langle r-R \rangle$ are 0.0568 (A), 0.0619 (B), 0.0549 (C), and 0.0655 (D). Brightness records of the ABC images are more accurate than those of D, and thus we reasonably take the average colours of ABC to estimate a mean *r* – *R* offset of 0.0579 mag. After correcting the *R*-band curves of the quasar for this offset, we obtain the new records in Table 2. This machine-readable ASCII file at the CDS contains *r*-band magnitudes of the quasar images and the control star at 207 observing epochs (MJD–50 000). In Figure 1, we also display our new 4-year light curves.

**Fig. 2.** $D^2_{4,2}(\text{AD})$ dispersion spectra for a SMO model, using decorrelation lengths $\delta = 10, 15$ and 20 d. Each dispersion spectrum describes the values of $D^2_{4,2}(\text{AD})$ for a broad range of time lags after optimising the magnitude offsets for every lag. We also zoom into the region that includes the minima (box in the right top corner).

3. Time delays and microlensing signals

Previous efforts focused on early monitorings with a single telescope, trying to estimate delays between the image A and the other quasar images, $\Delta t_{\text{AX}} = t_{\text{A}} - t_{\text{X}}$ ($\text{X} = \text{B}, \text{C}, \text{D}$), and find microlensing signals (Dyrland 2019; Goicoechea & Shalyapin 2019)³. Here, we use the new light curves in Section 2 along with state-of-the-art curve-shifting algorithms to try to robustly measure the three independent time delays Δt_{AB} , Δt_{AC} , and Δt_{AD} . At the end of this section, we also discuss the intrinsic and extrinsic (microlensing) variability of the quasar.

There are several cross-correlation techniques to measure time delays between light curves containing microlensing variations (e.g. Liao et al. 2015, and references therein), and thus we considered two very different methods and models to obtain reliable results. First, we performed the AB, AC, and AD comparisons using the $D^2_{4,2}$ dispersion method (Pelt et al. 1996). This technique evaluates the dispersion between two different light curves for a range of time lags and flux-ratio model parameters. For given values of the time lag and model parameters, each data point in one of the two light curves is compared with magnitudes in the other curve at time separations shorter than a

³ Goicoechea & Shalyapin (2019) used the notation $\Delta t_{\text{AX}} = t_{\text{X}} - t_{\text{A}}$ rather than that defined in this paper and Dyrland (2019)

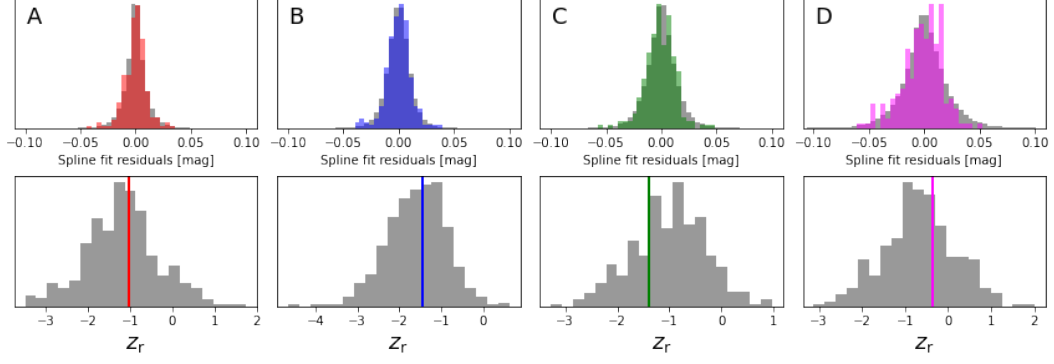


Fig. 3. *Top:* distributions of FKS fit residuals for $\eta = 50$ d and $\eta_{ml} = 400$ d. The grey histograms represent the distributions of residuals from the fits to 500 synthetic light curves of each image, while the red, blue, green and magenta histograms correspond to the distributions of residuals from the fits to the LT-NOT light curves. *Bottom:* normalized number of runs Z_r for the synthetic data (grey histograms) and the observed brightness records (red, blue, green and magenta vertical lines).

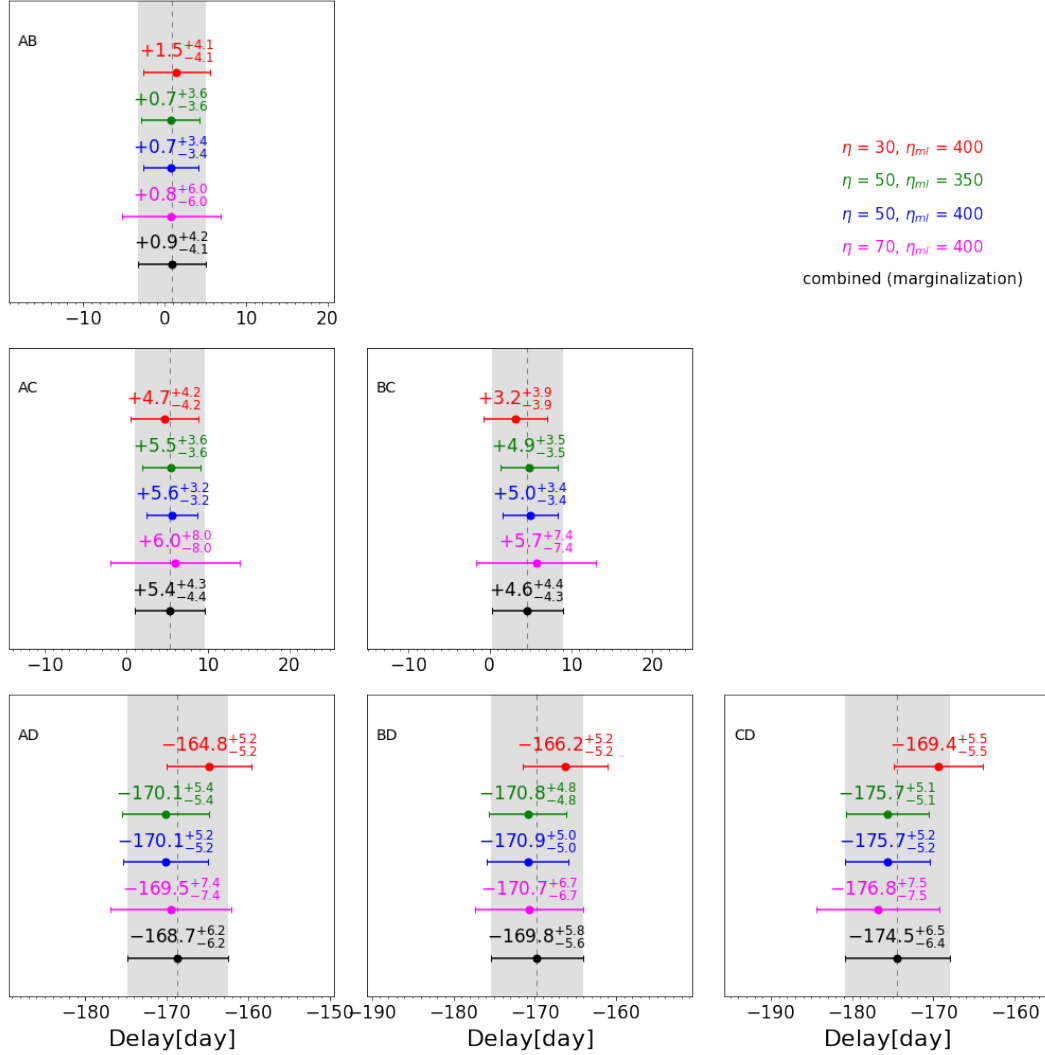


Fig. 4. Time-delay estimates using the χ^2 technique and free-knot splines. Combined estimates ($\tau_{\text{thresh}} = 0$; Bonvin et al. 2018) are highlighted with grey rectangles encompassing the individual measurements.

decorrelation length δ , and squared differences between pairs of data with longer separations and larger photometric errors have smaller weights. The key idea of the method is to find the time lag and model parameters that minimises the dispersion, i.e. the weighted sum of squared differences.

Our flux ratio model accounted for microlensing variability by incorporating four magnitude offsets instead a single one. In order to match the light curve of the reference image A and the shifted curve of another quasar image, the curve of A was split into four one-year segments, covering one observing sea-

son each. We then assumed a constant magnitude offset within every segment, while the offset was allowed to vary from one segment to other. This seasonal magnitude offset (SMO) model works well in presence of intra-year microlensing events and microlensing variability on timescales of several years (Goicoechea & Shalyapin 2016; Shalyapin et al. 2021). We have written a Python code to minimise the $D_{4,2}^2(\text{AB})$, $D_{4,2}^2(\text{AC})$, and $D_{4,2}^2(\text{AD})$ dispersions, and used three reasonable δ values of 10, 15 and 20 d. This 10-d interval of δ permits us to account for the intrinsic variance of the technique. Figure 2 displays the three dispersion spectra for the AD comparison.

We also carried out 1000 "repetitions of the experiment" by generating 1000 synthetic light curves of each image, performing AB, AC, and AD comparisons from these simulated curves, and obtaining the distributions of time lags and magnitude offsets that minimise dispersions (e.g. Goicoechea & Shalyapin 2019, and references therein). For example, the 1σ confidence intervals for Δt_{AD} through the corresponding time lag distributions are: -166.1 ± 9.5 , -166.3 ± 8.5 , and -166.3 ± 8.4 d for $\delta = 10$, 15, and 20 d, respectively. These measurements indicate that the intrinsic variance is well below the uncertainties, so hereafter we show only results for $\delta = 15$ d. The 1σ confidence intervals for Δt_{AB} , Δt_{AC} , and Δt_{AD} are listed in Table 3.

Table 3. Time delays of PS J0147+4630.

Method/model	Δt_{AB}	Δt_{AC}	Δt_{AD}
$D_{4,2}^2/\text{SMO}$	-1.0 ± 1.8	$+4.5 \pm 3.6$	-166.3 ± 8.5
χ^2/FKS	$+0.9 \pm 4.2$	$+5.4 \pm 4.4$	-168.7 ± 6.2
Combined	0 ± 3	$+5 \pm 4$	-167.5 ± 7.4

Note: When applying the $D_{4,2}^2$ dispersion, we consider a SMO model without assumptions about the intrinsic variability. We also use the χ^2 technique along with a FKS model to describe the intrinsic and extrinsic variations. Additionally, we combine $D_{4,2}^2/\text{SMO}$ and χ^2/FKS delays in a simple way, i.e. calculating mean central values and mean errors. We adopt these averages for subsequent studies. Here, Δt_{AX} ($X = \text{B, C, D}$) are in days, image A leads image X if $\Delta t_{\text{AX}} < 0$ (otherwise A trails X), and all measurements are 68% confidence intervals.

Second, the time delays of PS J0147+4630 were inferred from PyCS3 curve-shifting algorithms⁴ (Tewes et al. 2013; Millon et al. 2020a,b). PyCS3 is a software toolbox to estimate time delays between images of gravitationally lensed quasars, and we focused on the χ^2 technique, assuming that the intrinsic signal and the extrinsic ones can be modelled as a free-knot spline (FKS). This technique shifts the four light curves simultaneously (ABCD comparison) to better constrain the intrinsic variability, and relies on an iterative nonlinear procedure to fit the four time shifts and splines that minimise the χ^2 between the data and model (Tewes et al. 2013). Results depend on the initial guesses for the time shifts, so it is necessary to estimate the intrinsic variance of the method using a few hundred initial shifts randomly distributed within reasonable time intervals. In addition, a FKS is characterised by a knot step, which represents the initial spacing between knots. The model consists of an intrinsic spline with a knot step η and four independent extrinsic splines with η_{ml} that account for the microlensing variations in each quasar image (Millon et al. 2020b).

To address the intrinsic variability, we considered three η values of 30, 50 and 70 d. Intrinsic knot steps shorter than 30 d fit the observational noise, whereas η values longer than 70 d do not fit the most rapid variations of the source quasar. Intrinsic

variations are usually faster than extrinsic ones, and additionally, the software works fine when the microlensing knot step is significantly longer than η . Therefore, the microlensing signals were modelled as free-knot splines with $\eta_{\text{ml}} = 350\text{--}400$ d (i.e. values intermediate between those shown in Table 2 of Millon et al. 2020b). We also generated 500 synthetic (mock) light curves of each quasar image, optimised every mock ABCD dataset, and checked the similarity between residuals from the fits to the observed curves and residuals from the fits to mock curves. The comparison of residuals was made by means of two statistics: standard deviation and normalised number of runs Z_r (see details in Tewes et al. 2013). For $\eta = 50$ d and $\eta_{\text{ml}} = 400$ d, histograms of residuals derived from mock curves (grey) and from the LT-NOT light curves of PS J0147+4630 are included in the top panels of Figure 3. It is apparent that the standard deviations through the synthetic and the observed curves match very well. Additionally, the bottom panels of Figure 3 show distributions of Z_r from synthetic light curves (grey) for $\eta = 50$ d and $\eta_{\text{ml}} = 400$ d. These bottom panels also display the Z_r values from the observations (vertical lines), which are typically located at $\sim 0.3\sigma$ of the mean values of the synthetic distributions.

Four pairs of (η, η_{ml}) values (see above) led to the set of time delays in Figure 4. We have verified that other feasible choices for η_{ml} (e.g. $\eta_{\text{ml}} = 200$ d) do not substantially modify the results in this figure. The black horizontal bars correspond to 1σ confidence intervals after a marginalisation over results for all pairs of knot steps, and those in the left panels of Figure 4 are included in Table 3. We finally adopted the time delays in the fourth row of Table 3, which were obtained by averaging central values and errors in the two previous rows. It seems to be difficult to accurately determine delays between the brightest images ABC because they are really short. To robustly measure Δt_{AB} and Δt_{AC} in a near future, we will most likely need to follow a non-standard strategy focused on several time segments associated with strong intrinsic variations and weak extrinsic signals. Fortunately, we find an accurate and reliable value of Δt_{AD} (uncertainty of about 4%), confirming the early result by Dyrland (2019).

After building median-subtracted light curves, the central values of the adopted time delays (see Table 3) were used to shift in time such normalised curves. As A is the reference image and $\Delta t_{\text{AB}} = 0$, the new curves of A and B retained their original epochs. We then applied the PyCS3 software (χ^2/FKS model) to simultaneously fit the intrinsic signal and the microlensing variability of each quasar image. Figure 5 displays our results for $\eta = 30$ d and $\eta_{\text{ml}} = 400$ d (left panel), and $\eta = 70$ d and $\eta_{\text{ml}} = 200$ d (right panel). The black lines with knot vertical ticks model the intrinsic variation shared by the four light curves. Both intrinsic signal reconstructions are compared with microlensing-corrected and time-shifted normalised curves (circles). The blue, orange, green, and red lines model the microlensing variations of A, B, C, and D, respectively. The A image is weakly affected by microlensing, while the other three images show microlensing episodes with total amplitudes exceeding 0.05 mag, and the extrinsic variation of C is particularly prominent. We note that the two pairs of (η, η_{ml}) values we use in Figure 5 lead to similar delays between A and D (both consistent with the adopted one), but they produce microlensing splines for D (red lines) having different behaviours on time scales of hundreds of days.

We also considered the adopted time delays to fit seasonal magnitude offsets between image A and the other three images ($D_{4,2}^2/\text{SMO}$ model). In the left panel of Figure 6, we show the overlaps between the A data and the magnitude- and time-shifted curves of BCD. It is noteworthy that there is a significant overlap

⁴ <https://gitlab.com/cosmograil/PyCS3>

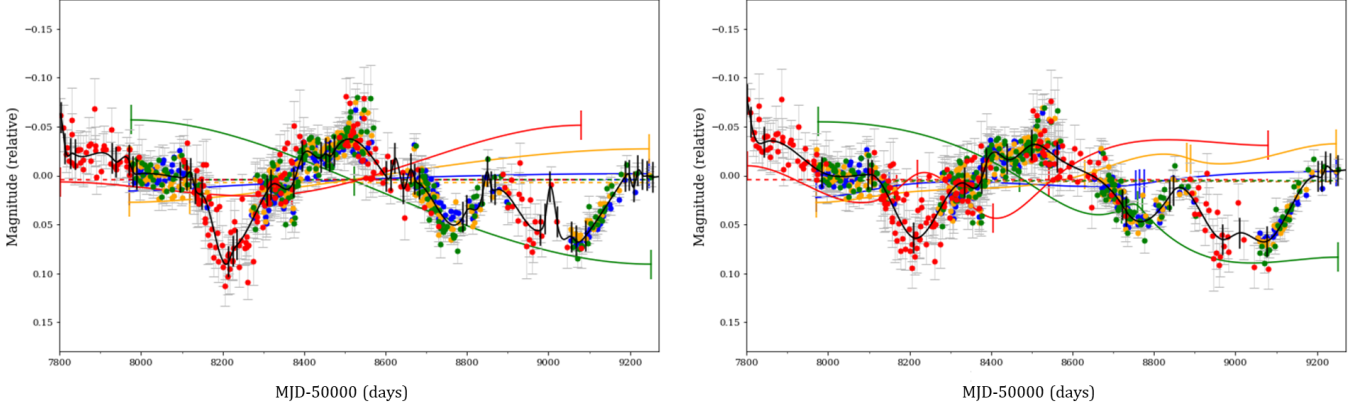


Fig. 5. Free-knot spline fits of the LT-NOT data of PS J0147+4630. The black lines depict the intrinsic splines, and the blue, orange, green, and red lines represent the splines for the microlensing variations of A, B, C, and D, respectively. Knots are shown as vertical ticks, whereas the horizontal dashed lines are references for microlensing. The intrinsic splines trace reasonably well the ensembles of circles: microlensing-corrected and median-subtracted light curves of the reference image A (blue), along with microlensing-corrected, time-shifted, and median-subtracted light curves of B (orange), C (green), and D (red). The curves of BCD are shifted in time by the adopted time delays (see Table 3), and all curves are corrected from their microlensing splines. *Left:* $\eta = 30$ d, $\eta_{\text{ml}} = 400$ d. *Right:* $\eta = 70$ d, $\eta_{\text{ml}} = 200$ d.

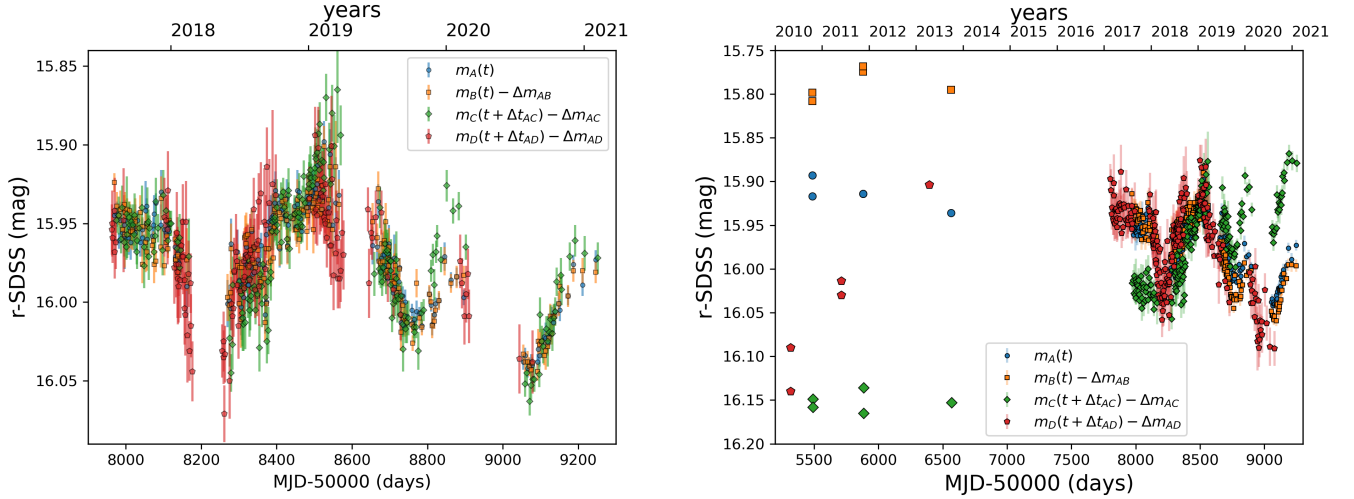


Fig. 6. Shifted light curves in the r band. *Left:* LT-NOT data. Overlapping between A original data and shifted data of BCD. To properly shift the BCD light curves, we consider the adopted time delays and corresponding seasonal magnitude offsets from the SMO model (see main text). *Right:* LT-NOT data plus photometric data from Pan-STARRS frames in 2010–2013. The original brightness record of A is compared with shifted light curves of B ($\Delta m_{AB} = -0.264$ mag), C ($\Delta t_{AC} = +5$ d, $\Delta m_{AC} = -0.590$ mag), and D ($\Delta t_{AD} = -167.5$ d, $\Delta m_{AD} = -2.304$ mag). The curve of B is not shifted in time because $\Delta t_{AB} = 0$ (see main text for details).

between the original curve of A and the shifted curve of D (see also Figure 5), supporting the reliability of the Δt_{AD} measurements in Table 3. In addition to an image comparison spanning four years, a comparison over an 11-year period is depicted in the right panel of Figure 6. We have downloaded five r -band warp frames of PS J0147+4630 that are included in the Data Release 2 of the Pan-STARRS. These Pan-STARRS frames were obtained on three nights in the 2010–2013 period, i.e. a few years before the discovery of the lens system. Two frames are available on two of the three nights, so rough photometric uncertainties through average intranight variations are 0.012 (A), 0.008 (B), 0.019 (C), and 0.033 (D) mag. To discuss the differential microlensing variability of the images BCD with respect to A, the right panel of Figure 6 shows the original curve of A along with shifted curves of BCD. We used the adopted time delays and arbitrary (con-

stant) magnitude offsets to shift curves. The shapes of the four brightness records indicate the presence of long-term microlensing effects and suggest that PS J0147+4630 is a suitable target for a deeper analysis of its microlensing signals.

4. Quasar redshift and image flux ratios from recent spectroscopic data

Rubin et al. (2018) estimated the redshift of PS J0147+4630 by cross-correlating a quasar spectral template with spectra of the four quasar images at wavelengths shorter than 5500 Å. This blue spectral region contains emission lines that are severely affected by absorption features, and even excluding the Ly α and N v lines, Rubin et al. obtained an inaccurate redshift $z_s = 2.377 \pm 0.007$ for the BAL quasar. The C III] emission of the broad

Table 5. Redshift and single-epoch image flux ratios of PS J0147+4630.

Emission	z_s	B/A	C/A	D/A
Mg II	2.355	—	—	0.065 ± 0.001
cont@2800	—	—	—	0.113 ± 0.001
H β	—	0.450 ± 0.012	0.263 ± 0.010	0.065 ± 0.003
[O III]	2.357	—	—	—
[O III] λ 5007	—	0.559 ± 0.038	0.311 ± 0.037	0.072 ± 0.017
cont@5100	—	0.593 ± 0.012	0.423 ± 0.008	0.122 ± 0.005
H α main	2.359	0.484 ± 0.003	0.292 ± 0.002	0.064 ± 0.001
H α VBC	—	0.541 ± 0.007	0.406 ± 0.005	0.068 ± 0.003
cont@6563	—	0.636 ± 0.002	0.435 ± 0.001	0.152 ± 0.001

Note: The Mg II and cont@2800 (continuum at $\lambda_{\text{rest}} = 2800 \text{ \AA}$) emissions are derived from the multi-component decomposition of Keck-ESI spectra (see the right panel of Figure 7). The H β , [O III], cont@5100 (continuum at $\lambda_{\text{rest}} = 5100 \text{ \AA}$), H α , and cont@6563 (continuum at $\lambda_{\text{rest}} = 6563 \text{ \AA}$) emissions are inferred from multi-component decompositions of GTC-EMIR spectra (see Figures 10 and 11).

absorption-line quasar is observed at $\sim 6400 \text{ \AA}$, and Lee (2017) measured $z_s = 2.341 \pm 0.001$ using only such emission line, which is apparently free of significant absorption-induced distortions. In this section, we analyse several emission lines at longer wavelengths, checking the reliability of the current value of z_s and trying to get information on image flux ratios.

The Keck Observatory Archive includes relevant data of PS J0147+4630 on 1 December 2018 (MJD–50 000 = 8453)⁵. These deep spectroscopic observations with the Echelle Spectrograph and Imager (ESI; Sheinis et al. 2002) consisted of $3 \times 2400 \text{ s}$ exposures using an $1''.0$ -width slit with a spatial pixel scale of $0''.154$. The slit was oriented along the line joining A and D. In addition, the ESI wavelength range and its resolving power were $3900\text{--}10\,500 \text{ \AA}$ and 4000, respectively. We downloaded the exposures of the lens system and spectroscopic data of the standard star Feige 110, as well as CuAr, Xe, and HgNe lamps exposures for wavelength calibration. Data reduction and spectral extraction were then performed using the MAUNA KEA Echelle Extraction (MAKEE) package by Tim Barlow⁶. To extract the individual spectra of A and D from the MAKEE software, we considered two apertures with 7 pixel size, which are similar to the slit width and the FWHM seeing. The normalised spectrum of the standard star allowed us to calibrate in flux and correct by telluric absorption the quasar spectra.

The final spectra of A and D are available in tabular format at the CDS: Table 4 includes fluxes of both quasar images covering the spectral range $3900\text{--}10\,500 \text{ \AA}$ with 33 001 channels of 0.2 \AA each. The Keck-ESI spectra of the two images are also plotted in the left panel of Figure 7. These new spectra show emission lines that were previously detected at visible wavelengths (Lee 2017; Rubin et al. 2018) and the Mg II line at $\sim 9400 \text{ \AA}$. Thus, we focused on the analysis of the Mg II line spectral region using a decomposition into three components: power-law continuum, Fe II pseudo-continuum, and Gaussian Mg II emission (see the right panel of Figure 7). The two Gaussian distributions (A and D) led to an unbiased redshift $z_s = 2.355$. Additionally, the D/A flux ratios for the pure Mg II emission and the continuum at $\lambda_{\text{rest}} = 2800 \text{ \AA}$ are given in Table 5. Uncertainties in these flux ratios (1σ confidence intervals) were estimated from 300 repetitions of each spectrum. To obtain synthetic spectra for A and D, we

modified the observed fluxes by adding realizations of normal distributions around zero, with standard deviations equal to the measured errors.

Recent spectroscopic observations of PS J0147+4630 with the near-IR instrument EMIR (Garzón et al. 2016) on the 10.4 m Gran Telescopio Canarias (GTC) are useful tools to discuss the H β , [O III], and H α emissions from the distant quasar. These data were taken on 14 August 2019 (MJD–50 000 = 8709) under excellent seeing conditions (FWHM seeing $\sim 0''.6$) and are available at the GTC Public Archive⁷. The $0''.6$ -width slit was oriented along two different directions (see Figure 8): one crossing the ABC images (slit orientation 1; total exposure time of $1920 \text{ s} = 12 \times 160 \text{ s}$), and the other crossing the AD images and the lens galaxy G (slit orientation 2; total exposure time of $3840 \text{ s} = 24 \times 160 \text{ s}$). The spatial pixel scale was $0''.1915$, while the EMIR-HK pseudo-grism wavelength range and resolving power were $1.45\text{--}2.42 \text{ \mu m}$ and 987, respectively. There are also observations of the standard telluric star HIP10814 on the same night.

We downloaded the GTC-EMIR data and used the PyEMIR software (Cardiel et al. 2019) for their reduction. For each slit orientation, we extracted three individual spectra (ABC or ADG) by fitting three 1D Moffat profiles in the spatial direction for each wavelength bin (e.g. Sluse et al. 2007; Shalyapin & Goicoechea 2017; Goicoechea & Shalyapin 2019). To fit the Moffat profiles, the positions of BCDG with respect to A were set from the HST astrometry of the system (Shajib et al. 2019, 2021). Spectra were calibrated in flux, and telluric absorption was properly corrected. In addition, we have taken into account slit losses (relative to A) of 0.928 (B), 0.932 (C), and 0.995 (D) because the BCD images are not centred on the slit axis (see Figure 8). A 1D Moffat profile does not account for the total light of the very faint galaxy G and the slit loss of G is not taken into account either. In this study, we are interested in the quasar spectra and warn that fluxes of G are underestimated. Final spectra for the slit orientations 1 and 2 are shown in Tables 6 and 7, respectively. Both tables are available at the CDS and are structured in a similar way. Table 6 includes wavelengths in \AA and fluxes of ABC, whereas Table 7 includes the same wavelengths and fluxes of ADG. All fluxes are given in $10^{-17} \text{ erg cm}^{-2} \text{ s}^{-1} \text{ \AA}^{-1}$. Figure 9 also displays the new near-IR spectra of PS J0147+4630.

⁵ <https://koa.ipac.caltech.edu/cgi-bin/KOA/nph-KOALogin> (Program ID: U122, Program PI: C. Fassnacht)

⁶ <https://sites.astro.caltech.edu/~tb/makee>

⁷ <https://gtc.sdc.cab.inta-csic.es/gtc/> (Program ID: GTCMULTIPLE2B-19B, Program PI: R. Scarpa)

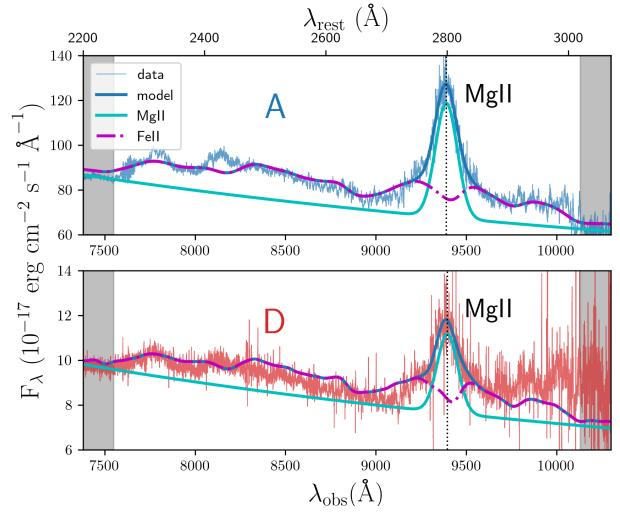
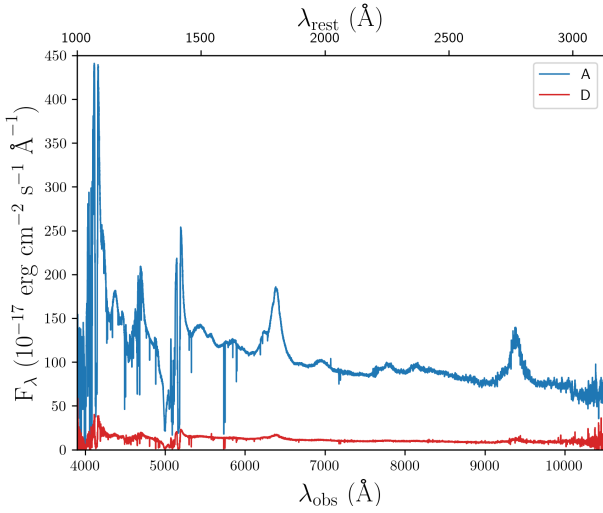


Fig. 7. *Left:* Keck-ESI spectra of PS J0147+4630AD in December 2018. *Right:* multi-component decomposition of the Mg II line spectral region in the Keck-ESI spectra (see main text). The pure Mg II emission is modelled as a Gaussian function, and the two Gaussian distributions (A and D) with rest-frame central wavelengths of ~ 2800 Å (vertical dotted lines) are drawn superimposed on power-law continua.

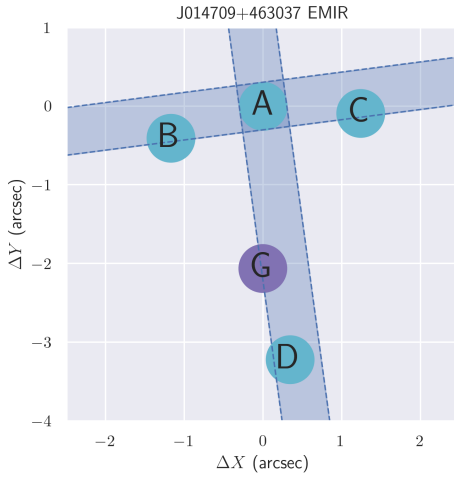


Fig. 8. Positions of the four images and the lens galaxy of PS J0147+4630 on the two slit orientations for GTC-EMIR. Using the almost horizontal slit (orientation 1), it is possible to obtain spectra of ABC. The almost vertical slit (orientation 2) is suitable for extracting spectra of ADG. The circles represent seeing discs (diameter = FWHM seeing).

The GTC-EMIR quasar spectra cover the wavelength range of H β , [O III], and H α emission lines. At λ_{rest} around 4900 Å, these spectra were modelled as the sum of a power-law continuum, a Fe II pseudo-continuum, and three Gaussian emissions of H β , [O III] $\lambda 4959$, and [O III] $\lambda 5007$ (see Figure 10). From the [O III] doublet, we determined the optimal redshift $z_s = 2.357$. Flux ratios were also estimated and incorporated in Table 5. To account for the shape of the H α emission at rest-frame wavelengths around 6500 Å, we considered a decomposition into three components: power-law continuum and two Gaussian H α emissions (see Figure 11), i.e. a main component (the average FWHM of the velocity distributions is ~ 4900 km s $^{-1}$) and a very broad component (VBC; the average FWHM velocity is $\sim 22\,300$ km s $^{-1}$) that is blueshifted with respect to the main one by 5000–9000 km s $^{-1}$. The source redshift from the main component and several flux ratios are shown in Table 5. Uncer-

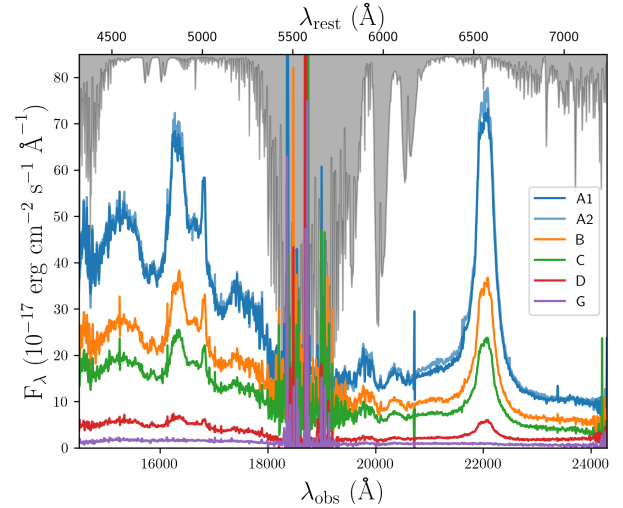


Fig. 9. GTC-EMIR spectra of PS J0147+4630 in August 2019. Spectra A1, B, and C correspond to the slit orientation 1, and spectra A2, D, and G are associated with the slit orientation 2 (see Figure 8). The grey line describes the atmospheric transmission. Water and carbon dioxide completely block transmission of light at ~ 1.9 μm .

tainties in flux ratios from GTC-EMIR data were derived from 300 repetitions of the experiment (synthetic spectra based on the observed ones; see above). To generate simulated spectra of a quasar image, we previously estimated spectral errors as absolute differences between the measured fluxes and those in a smoothed version of its observed spectrum.

Our detailed analysis of emission lines detected at near-IR wavelengths suggests that $z_s = 2.357 \pm 0.002$ (see Table 5). This is basically the average of previous redshifts based on visible spectra, and reported by Lee (2017) and Rubin et al. (2018). The single-epoch image flux ratios in Table 5 are also worthy of attention. We find that all flux ratios for emission lines are smaller than those for continuum emissions at wavelengths inside or near wavelength ranges of lines. Lee (2018) also indicated that the D/A flux ratio for the C III] emission line is smaller than that for its underlying continuum. This previous result, which was interpreted as evidence of spectral microlensing, is fully consistent

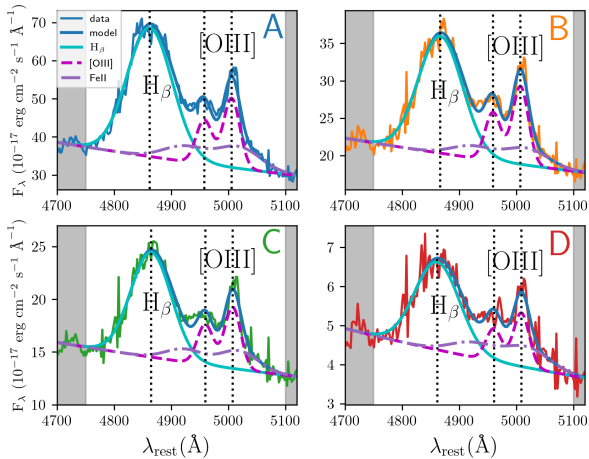


Fig. 10. Multi-component decomposition of the $H\beta$ + $[O\text{ III}]$ complex spectral region in the GTC-EMIR spectra (the spectrum of A is the average of A1 and A2 in Figure 9; see main text). Each of the $H\beta$, $[O\text{ III}]\lambda 4959$, and $[O\text{ III}]\lambda 5007$ emissions is modelled as a Gaussian function. All Gaussian distributions are drawn superimposed on power-law continua, and their rest-frame central wavelengths are highlighted with vertical dotted lines.

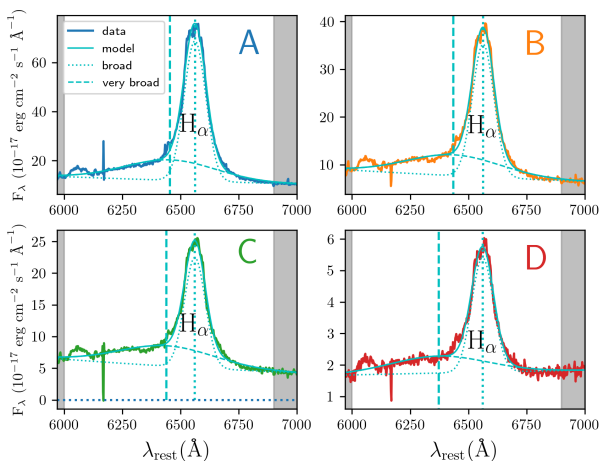


Fig. 11. Multi-component decomposition of the $H\alpha$ line spectral region in the GTC-EMIR spectra (the spectrum of A is the average of A1 and A2 in Figure 9; see main text). The main (broad component) and VBC $H\alpha$ emissions are both modelled as a Gaussian function. The Gaussian distributions are drawn superimposed on power-law continua, and their rest-frame central wavelengths are highlighted with dotted vertical lines (main component) and dashed vertical lines (VBC).

with new data in the last column of Table 5. Additionally, the VBC $H\alpha$ emission is most likely due to an outflow in the BAL quasar, which is not detected in the $H\beta$ emission. We also note that possible extended blue wings of the $[O\text{ III}]$ lines cannot be resolved with available observations. Our data suggest a possible link between the outflow related to absorption features in high-ionization emission lines ($\text{Ly}\alpha$, N V and C IV ; Rubin et al. 2018) and the VBC $H\alpha$ emission.

At the end of Section 5, flux ratio measurements in Table 5 are compared with macrolens flux ratios predicted by an updated lens mass model, which permits us to discuss extinction/microlensing scenarios. Some results of this discussion are

used to confidently estimate the quasar black hole mass in Section 6.

5. Lens mass model

Berghea et al. (2017) presented preliminary modelling of the lens mass of PS J0147+4630 from Pan-STARRS data, whereas Shajib et al. (2019, 2021) have recently modelled the lens system using HST imaging. Shajib et al.'s solution for the lensing mass relies on a lens scenario consisting of a singular power-law ellipsoid (SPLE; describing the gravitational field of the main lens galaxy G) and an external shear (ES; accounting for the gravitational action of other galaxies). The dimensionless surface mass density (convergence) profile of the SPLE was characterised by a power-law index β , and they found $\beta = 2.00 \pm 0.05$, where $\beta = 2$ for an isothermal ellipsoid⁸.

Assuming a flat Λ CDM cosmology with matter and dark energy densities of $\Omega_M = 0.3$ and $\Omega_\Lambda = 0.7$, respectively⁹, we first considered Shajib et al.'s solution, updated redshifts $z_1 = 0.678$ (Goicoechea & Shalyapin 2019) and $z_s = 2.357$ (see Section 4), and our longest (most accurate) time delay in the fourth row of Table 3 to calculate H_0 and put it into perspective (e.g. Jackson 2015). Using the measured delay between images A and D, the Hubble constant is $102 \pm 11 \text{ km s}^{-1} \text{ Mpc}^{-1}$, in clear disagreement with currently accepted values around $H_0 = 70 \text{ km s}^{-1} \text{ Mpc}^{-1}$. If additional mass along the line of sight is modelled as an external convergence κ_{ext} , the factor $1 - \kappa_{\text{ext}}$ should be ~ 0.7 ($\kappa_{\text{ext}} \sim 0.3$) to decrease H_0 until accepted values. Therefore, the external convergence required to solve the delay crisis is an order of magnitude higher than typical values of κ_{ext} (e.g. Rusu et al. 2017; Birrer et al. 2020).

To better understand the reasons for the crisis of Shajib et al.'s solution when measured time delays are taken into account, the system was also modelled using astrometric and time-delay constraints, an SPLE + ES mass model, updated redshifts, a flat Λ CDM cosmology, and $H_0 = 70 \text{ km s}^{-1} \text{ Mpc}^{-1}$. Thus, even in presence of a standard (weak) external convergence, the H_0 value would be consistent with accepted ones. We have downloaded the four HST-WFC3 frames that were used by Shajib et al.¹⁰, and then determined positions of ABCDG in each of them through the IRAF/FITPSF/ELGAUSS task. We also considered the Gaia EDR3 positions of the quasar images¹¹ (Lindgren et al. 2021). The Gaia-HST imaging allowed us to obtain the astrometric constraints in Table 8, consisting of positions of BCDG with respect to A at the origin of coordinates. Table 8 shows means and standard errors of means from the five (four) independent solutions for the coordinates of BCD (G), so typical statistical uncertainties are $0''.0008$ (coordinates of BCD) and $0''.006$ (coordinates of G).

Each set of observational constraints (SOC) included the three combined time delays in Table 3. In addition to these three constraints, the first set (SOC 1) incorporated the HST relative positions of ABCD (with respect to G at the origin of coordinates; Shajib et al. 2019, 2021), while the second (SOC 2) contained the Gaia-HST astrometry in Table 8. When building

⁸ More precisely, the original name of the power-law index in Shajib et al. (2019, 2021) was γ , but we have renamed it as β to avoid confusion between such index and the shear

⁹ Results do not change appreciably for values of Ω_M and Ω_Λ slightly different from those adopted here

¹⁰ <https://archive.stsci.edu/missions-and-data/hst> (Program ID: 15320, Program PI: T. Treu)

¹¹ <https://gea.esac.esa.int/archive/>

Table 8. Astrometric solution from Gaia-HST data of PS J0147+4630.

Component	x	y
B	-1.1683 ± 0.0003	-0.4137 ± 0.0008
C	1.2432 ± 0.0011	-0.0988 ± 0.0008
D	0.3383 ± 0.0010	-3.2343 ± 0.0005
G	0.1632 ± 0.0055	-2.0562 ± 0.0062

Note: The A image is at the origin of coordinates (0, 0), and positive directions of x and y are defined by west and north, respectively. Both x and y are given in arcseconds.

Table 9. Solutions for the SPLE + ES mass model of PS J0147+4630.

Parameter	SOC 1	SOC 2
$\chi^2/\text{d.o.f.}$	4.0/3	3.2/3
β	1.83	1.845 ± 0.070
b (")	1.88	1.882 ± 0.016
e	0.165	0.151 ± 0.041
θ_e (°)	-71.5	-67.5 ± 4.8
γ	0.174	0.166 ± 0.019
θ_γ (°)	10.9	11.5 ± 0.7

Note: When fitting the SPLE + ES mass model, we consider updated lens and source redshifts, a flat Λ CDM cosmology, $H_0 = 70 \text{ km s}^{-1} \text{ Mpc}^{-1}$, and two different sets of observational constraints (SOC 1 and SOC 2; see main text). Position angles (θ_e and θ_γ) are measured east of north, and $\chi^2/\text{d.o.f.}$, β , b , e , and γ denote reduced chi-square, power-law index, mass scale and ellipticity of the SPLE, and external shear strength, respectively.

the SOC 1, we considered the Shajib et al.'s astrometric uncertainties for ABCD, i.e. the original ones. In the SOC 2, we assumed $\sigma_x = \sigma_y = 0''.0008$ for BCD (see above). SPLE + ES mass models of quads usually indicate the existence of an offset between the centre of the SPLE and the light centroid of the galaxy (e.g. Sluse et al. 2012; Shajib et al. 2019, 2021). Hence, instead of formal astrometric errors for G, we initially adopted $\sigma_x = \sigma_y = 0''.04$ in both SOC 1 and SOC 2. This uncertainty level equals the root-mean-square of mass/light positional offsets for most quads in the sample of Shajib et al. The number of observational constraints and the number of model parameters were 13 and 10, respectively. For three degrees of freedom (d.o.f.), the GRAVLENS/LENMODEL software¹² (Keeton 2001, 2004) led to the best fit (SOC 1) and 1σ intervals (SOC 2) in Table 9. Additionally, Figure 12 depicts the χ^2 - β and χ^2 - θ_γ relationships from the SOC 2.

The SOC 1 and SOC 2 produce similar parameter values, and hereafter we focus on results from the SOC 2 because it leads to a better fit in terms of the reduced chi-square. Regarding the mass of the early-type galaxy G, it is clear that a convergence a little shallower than isothermal ($\beta < 2$) is required to reasonably fit the measured time delays when $H_0 = 70 \text{ km s}^{-1} \text{ Mpc}^{-1}$ (see Table 9 and the top panel of Figure 12). Additionally, our values of the mass scale and ellipticity ($e = 1 - q$, where q is the axis ratio) agree with those in Table 3 of Shajib et al., and the new orientation of G (θ_e) does not differ substantially from the previous one. Therefore, there is still a high misalignment angle between light and mass distributions. This misalignment may be true or an artefact arising from the SPLE + ES scenario that we and Shajib et al. assumed. Despite the new external shear orientation (θ_γ) is almost perpendicular to that of Shajib et al. (see the bottom panel of Figure 12), the external shear strength around

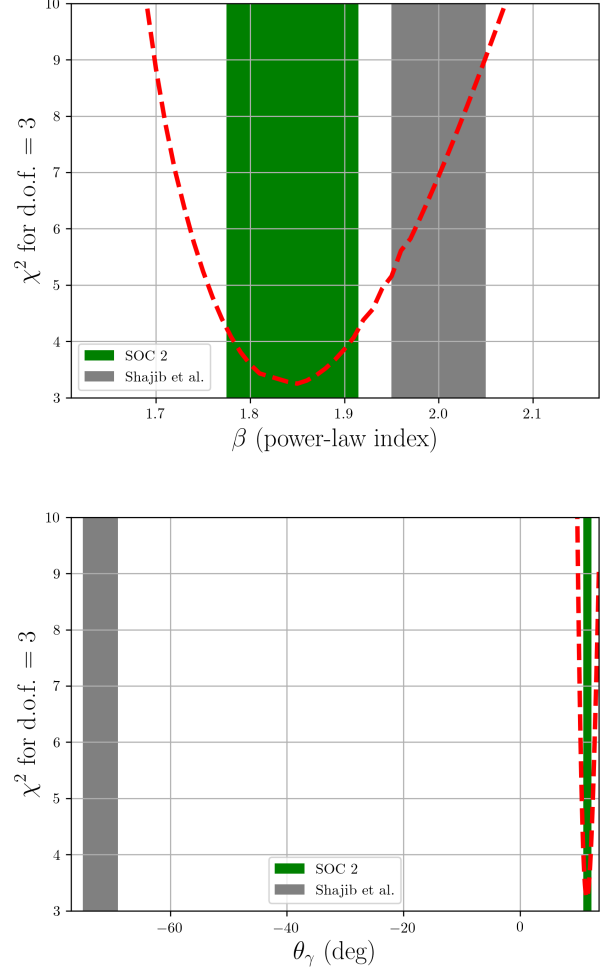


Fig. 12. Some results of lens mass modelling of PS J0147+4630. Our 1σ intervals from the SOC 2 (see Table 9; green rectangles) are compared with those of Shajib et al. (grey rectangles). *Top*: power-law index of the SPLE ($\beta = 2$ for an isothermal distribution). *Bottom*: position angle of the ES.

0.166 in Table 9 coincides with the previous one. Most early-type galaxies reside in overdense regions, so external tidal fields in their vicinity are expected to have relatively high amplitudes. External shear strengths for quads exceeding 0.1 are consistent with N-body simulations and semianalytic models of galaxy formation (Holder & Schechter 2003). Using a model consisting of a singular isothermal elliptical potential and external shear, Luhtaru et al. (2021) have also shown that PS J0147+4630 is a shear-dominated system.

Using constraints from HST imaging, Shajib et al. (2019, 2021) found a mass/light positional offset for G exceeding $0''.1$ (see Fig. 5 in that paper). However, our solution from the SOC 2 suggests a positional offset of $\sim 0''.06$ (see Figure 13), which is one half of that by Shajib et al., but still noticeably large. This new offset is about 10 times the formal uncertainties σ_x and σ_y for G (see above). Shajib et al. have briefly commented on the existence of nearby companions of G, which could fix the issue. For example, Sluse et al. (2012) reported that "astrometric anomalies" of many quads are solved by explicitly incorporating the nearest galaxy/group to the main lens into the lens model. The astrometric anomaly of PS J0147+4630 might also be related to the substructure and azimuthal shape of the mass distri-

¹² <http://www.physics.rutgers.edu/~keeton/gravlens/>

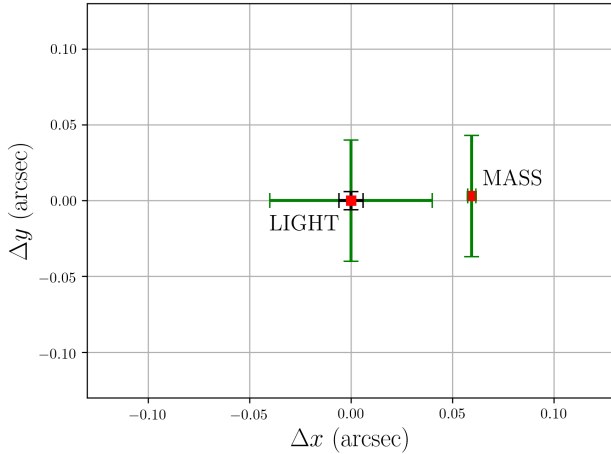


Fig. 13. Mass/light positional offset for the lens galaxy of PS J0147+4630. The observed (light) centroid of G is placed at the origin of coordinates, and its associated green and black bars describe adopted and formal uncertainties, respectively. The centre of the SPLE (mass distribution) is located at $\Delta x \sim 0''.6$ from the origin, and its associated green bars represent 1σ errors.

bution of G (e.g. Sluse et al. 2012; Gomer & Williams 2021). Alternatively, the displacement vector from the observed centroid to the centre of the mass distribution could be real instead of an artefact due to the mass model used (e.g. Shu et al. 2016).

Table 10. Predicted values of macrolens flux ratios and magnifications.

Parameter	SPLE + ES (SOC 2)
M_{BA}	0.561 ± 0.001
M_{CA}	0.567 ± 0.008
M_{DA}	0.056 ± 0.002
μ_A	36.4 ± 4.4
μ_B	20.4 ± 2.4
μ_C	20.6 ± 2.2
μ_D	2.03 ± 0.22

Note: Macrolens flux ratios $M_{XA} = F_X/F_A$ ($X = B, C, D$) and macrolens magnification (μ) of the four quasar images.

We may also consider the predicted macrolens flux ratios and magnifications in Table 10 as proxies for their true values. First, the M_{BA} and M_{DA} values in Table 10 are in good agreement with the B/A and D/A flux ratios for the $[O\text{III}]\lambda 5007$ emission line (see Table 5). This narrow forbidden line is most likely related to a quasar extended region that is unaffected by microlensing (e.g. Abajas et al. 2002). Additionally, regarding the narrow-line emitting region in PS J0147+4630, differential dust extinction at $\lambda_{\text{lens}} \sim 10\,000 \text{ \AA}$ does not seem to play a relevant role in image pairs AB and AD¹³. The situation is quite different, however, for the pair AC. The C image is probably crossing a dust-rich region of the lens galaxy, which would resolve the conflict between M_{CA} and C/A for the $[O\text{III}]\lambda 5007$ line.

Second, if we focus on the images A and B, the B/A flux ratio for the continuum at $\lambda_{\text{rest}} = 5100 \text{ \AA}$ (see Table 5) is only 4–8% above the value of M_{BA} in Table 10. Therefore, $B/A(\text{cont}@5100)$ is weakly affected by differential microlensing and differential dust extinction at $\lambda_{\text{lens}} = 10\,200 \text{ \AA}$ (the time delay between A

and B is extremely short). To account for the 4–8% excess, the two simplest scenarios are: (1) A is not affected by extinction/microlensing, i.e. we can adopt a galaxy transmission factor $\epsilon_{G,A} = 1$ for light emission at 5100 \AA and a total magnification equal to μ_A in Table 10, but B is suffering a slight microlensing magnification ($\epsilon_{G,B} = 1$ and total magnification $\alpha\mu_B$, where $\alpha = 1.06 \pm 0.02$ and μ_B is given in Table 10), and (2) B is not affected by extinction/microlensing ($\epsilon_{G,B} = 1$ and total magnification μ_B), but the dust of G is weakly affecting A or microlensing is demagnifying this image ($\epsilon_{G,A} \times \text{total magnification} = \mu_A/\alpha$).

6. Mass of the central black hole in the quasar

Assuming the two extinction/microlensing scenarios in the last paragraph of Section 5, we plausibly estimated the mass of the supermassive black hole at the centre of PS J0147+4630. Vestergaard & Peterson (2006) have reported a relationship between the central black hole mass in a quasar, the continuum luminosity at $\lambda_{\text{rest}} = 5100 \text{ \AA}$, and the FWHM of the $H\beta$ emission line, and we used their result to obtain $H\beta$ -based masses from the GTC-EMIR spectra of A and B in Section 4. While the $H\beta$ line widths, $\text{FWHM} = 5731 \text{ (A) and } 5588 \text{ (B) km s}^{-1}$, were used as they are, we adopted a flat Λ CDM cosmology with $H_0 = 70 \text{ km s}^{-1} \text{ Mpc}^{-1}$ to infer luminosities from continuum fluxes $F_{5100 \text{ \AA}} = 30.21 \text{ (A) and } 17.92 \text{ (B) in units of } 10^{-17} \text{ erg cm}^{-2} \text{ s}^{-1} \text{ \AA}^{-1}$, the corresponding galaxy transmissions and total magnifications, and the Milky Way transmission $\epsilon_{\text{MW}} = 0.95$ (see Eq. (1) in Shalyapin et al. 2021). The first extinction/microlensing scenario led to $\log [M_{\text{BH}}/M_\odot] = 9.31\text{--}9.36$ and $9.28\text{--}9.34$ for A and B, respectively. The second scenario yielded $\log [M_{\text{BH}}/M_\odot] = 9.32\text{--}9.37 \text{ (A) and } 9.30\text{--}9.35 \text{ (B)}$. Additionally, using Eq. (4) of Assef et al. (2011) to estimate $H\beta$ -based masses, the mass logarithm ranged from 9.30 to 9.40.

Assef et al. (2011) also proposed a correlation between M_{BH} , the continuum luminosity at $\lambda_{\text{rest}} = 5100 \text{ \AA}$, and the FWHM of the $H\alpha$ emission line. The line widths $\text{FWHM}_{H\alpha} = 4981 \text{ (A) and } 4943 \text{ (B) km s}^{-1}$ from the GTC-EMIR spectra, along with the continuum luminosities (see the previous paragraph) and Eq. (5) of Assef et al. (2011), provided confirmation of the $H\beta$ -based black hole masses. We obtained $\log [M_{\text{BH}}/M_\odot]$ values ranging between 9.29 and 9.37, in excellent agreement with those from the $H\beta$ line. Although our overall result is $\log [M_{\text{BH}}/M_\odot] = 9.34 \pm 0.06$, the scatter of ± 0.06 dex does not account for errors in line widths, continuum fluxes, and other physical quantities. Assef et al. showed (see their Table 5) that the true uncertainty in the logarithmic mass is four to five times larger than our scatter estimation. Thus, we finally adopted $\log [M_{\text{BH}}/M_\odot] = 9.34 \pm 0.30$.

In a Schwarzschild geometry, the event horizon of the central black hole would be located at a typical radius of $6.5 \times 10^{14} \text{ cm}$, whereas the innermost ring of the accretion disc would have a radius three times larger, i.e. $\sim 2 \times 10^{15} \text{ cm}$. Although the Event Horizon Telescope (EHT) has recently taken stunning radio images of the vicinity of the central supermassive black holes in the Milky Way and the local galaxy M87 (The EHT Collaboration et al. 2019, 2022), such tiny regions in distant galaxies cannot be resolved by direct imaging. Fortunately, inner regions of accretion discs in gravitationally lensed quasars can be spatially resolved by microlensing (e.g. Kochanek 2004; Fian et al. 2021a) and reverberation-mapping (e.g. Gil-Merino et al. 2012) studies. Thus, the microlensing variability observed for 14 lensed quasars provided a relationship between black hole mass and accretion disc radius at 2500 \AA (Morgan et al. 2018), which

¹³ λ_{lens} denotes wavelength in the lens rest-frame

yielded a radius of about 1.2×10^{16} cm for the 2500 Å continuum source of PS J0147+4630. Using the standard accretion disc model (Shakura & Sunyaev 1973), the measured black hole mass and predicted accretion disc size led to an Eddington factor $\log(L/\eta L_E) \sim 2$ (e.g. Morgan et al. 2010), suggesting a very low radiative efficiency $\eta \sim 0.01 (L/L_E)$.

7. Conclusions

In this paper, we performed a comprehensive analysis of the optical variability of the quadruply-imaged quasar PS J0147+4630. Well-sampled light curves from its discovery in 2017 to 2021 were used to robustly measure the time delay between the brightest image A and the faintest D (167.5 ± 7.4 d, A is leading). Unfortunately, these light curves did not allow us to accurately determine the very short time delays between the three bright images ABC forming a compact arc. Additionally, the A image was weakly affected by microlensing over the period 2017–2021, while the microlensing-induced variation of the C image was particularly large in that period. Combining our new brightness records with quasar fluxes from Pan-STARRS imaging in 2010–2013, the extended light curves also revealed significant long-term microlensing effects. A microlensing analysis of current data and future light curves from a planned optical multi-band monitoring is expected to lead to important constraints on the spatial structure of the quasar accretion disc (Eigenbrod et al. 2008; Poindexter et al. 2008; Cornachione et al. 2020; Goicoechea et al. 2020).

The GTC and Keck Observatory public archives contain unexplored near-IR spectroscopy of the lensed quasar PS J0147+4630 in 2018–2019. We extracted spectra for individual images from such near-IR observations, and then analysed in detail the Mg II, H β , [O III], and H α emission lines, as well as their associated continua. These emission lines cover the spectral range 0.9–2.4 μ m, are unaffected by absorption features, and were used to constrain the source (quasar) redshift in a reliable way. We obtained $z_s = 2.357 \pm 0.002$, which resolves the controversy over the z_s value through visible spectra (Lee 2017; Rubin et al. 2018). We also derived single-epoch image flux ratios for emission lines, and the continuum at quasar rest-frame wavelengths of 2800, 5100 and 6563 Å. Although a detailed analysis of the flux ratios in Table 5 is out of the scope of this paper, it might provide accurate measurements of macrolens flux ratios, and reveal details of the spectral microlensing and dust extinction in the system (e.g. Goicoechea & Shalyapin 2016; Shalyapin & Goicoechea 2017). Spectral microlensing is often used to probe the quasar structure (e.g. Sluse et al. 2007; Motta et al. 2012; Fian et al. 2021b). In addition, we detected a very broad component in the H α emission that is likely related to the outflow in the BAL quasar (Lee 2017; Rubin et al. 2018).

Using HST imaging of the quad, Shajib et al. (2019, 2021) have carried out reconstruction of the lensing mass from an SPLE + ES model. Adopting updated redshifts of the source and lens (see here above and Goicoechea & Shalyapin 2019), and assuming a standard cosmology with $H_0 \sim 70$ km s $^{-1}$ Mpc $^{-1}$, the Shajib et al.’s solution cannot reproduce the measured delay between images A and D. An unacceptably high value of H_0 or an unusual external convergence is required to account for our longest delay. All the previous mass models, including the most recent modelling of Schmidt et al. (2022), actually predict a delay between the brightest image and the faintest that exceeds the measured one by a factor of ~ 1.5 – 1.8 . To take a deeper look at the SPLE + ES mass model, we used Gaia-HST

astrometry and the measured delays as constraints. Updated redshifts and a standard cosmology with $H_0 = 70$ km s $^{-1}$ Mpc $^{-1}$ were also adopted. We found that the power-law index of the SPLE and the position angle of the ES disagree with those of the Shajib et al.’s solution. Although the Gaia-HST relative positions of quasar images and measured delays are well reproduced by the mass model, the light and mass distributions of the lens galaxy do not match. There is a significant mass/light misalignment that could be true or due to an oversimplification of the lens scenario (e.g. Sluse et al. 2012; Shu et al. 2016; Gomer & Williams 2021). Further refinement of the new lens mass model along with an extension/improvement of the set of observational constraints (delays, macrolens flux ratios, galaxy velocity dispersion, etc) will contribute to an accurate determination of H_0 and other cosmological parameters (e.g. Bonvin et al. 2017; Birrer et al. 2020).

Comparing macrolens flux ratios predicted by our lens model with measured flux ratios (see above), we checked the consistency of results and discussed some extinction/microlensing effects in the lens system. The narrow-line emitting region is expected to be free from microlensing effects (e.g. Abajas et al. 2002), although it could be affected by dust extinction. Indeed, the flux ratios for the [O III] λ 5007 emission line are consistent with the absence of microlensing and the presence of an important amount of dust in the region of the lens galaxy that is crossed by the C image. Additionally, the B/A flux ratio for the continuum at $\lambda_{\text{rest}} = 5100$ Å is very close to the macrolens flux ratio between images B and A. Hence, with regard to the continuum at $\lambda_{\text{rest}} = 5100$ Å, both images are presumably suffering weak extinction/microlensing effects, which allowed us to obtain a relatively narrow range of quasar luminosities from the fluxes of A and B. These luminosities, and the widths of the H β and H α emission lines for the two brightest images, led to an estimate of the black hole mass in the heart of the distant quasar (a black hole mass based on spectra of two quasar images in a quad was also derived by Melo et al. 2021). The mass of the black hole in PS J0147+4630 is similar to those measured in other quads from Balmer line widths (e.g. Cloverleaf quasar and Einstein Cross; Assef et al. 2011), but one of great relevance in constraining the relationship between accretion disc size and black hole mass at masses above $2 \times 10^9 M_\odot$ (see Fig. 9 of Morgan et al. 2018).

Acknowledgements. We thank Martin Millon for making publicly available a Jupiter notebook that has greatly facilitated the use of the PyCS3 software. We also thank an anonymous referee for her/his comments and suggestions, which have helped us to improve the original manuscript. This paper is based on observations made with the Liverpool Telescope (LT) and the Nordic Optical Telescope (NOT). The LT is operated on the island of La Palma by Liverpool John Moores University in the Spanish Observatorio del Roque de los Muchachos of the Instituto de Astrofísica de Canarias with financial support from the UK Science and Technology Facilities Council. The NOT is operated by the Nordic Optical Telescope Scientific Association at the Observatorio del Roque de los Muchachos, La Palma, Spain, of the Instituto de Astrofísica de Canarias. The data presented here were in part obtained with ALFOSC, which is provided by the Instituto de Astrofísica de Andalucía (IAA) under a joint agreement with the University of Copenhagen and NOTSA. We thank the staff of both telescopes for a kind interaction. This work is also based on spectroscopic data from the GTC Public Archive at CAB (INTA-CSIC), as well as the Keck Observatory Archive (KOA), which is operated by the W. M. Keck Observatory and the NASA Exoplanet Science Institute (NExScI), under contract with the NASA. We have also used imaging data taken from the Pan-STARRS archive, the Barbara A. Mikulski archive for the NASA/ESA Hubble Space Telescope, and the archive of the ESA mission Gaia, and we are grateful to all institutions developing and funding such public databases. HD acknowledges support from the Research Council of Norway. This research has been supported by the grant PID2020-118990GB-I00 funded by MCIN/AEI/10.13039/501100011033.

References

- Abajas, C., Mediavilla, E., Muñoz, J. A., Popović, L. Č., & Oscoz, A. 2002, *ApJ*, 576, 640
- Assef, R. J., Denney, K. D., Kochanek, C. S., et al. 2011, *ApJ*, 742, A93
- Berghea, C. T., Nelson, G. J., Rusu, C. E., Keeton, C. R., & Dudik, R. P. 2017, *ApJ*, 844, A90
- Birrer, S., Shajib, A. J., Galan, A., et al. 2020, *A&A*, 643, A165
- Bonvin, V., Courbin, F., Suyu, S. H., et al. 2017, *MNRAS*, 465, 4914
- Bonvin, V., Chan, J. H. H., Millon, M., et al. 2018, *A&A*, 616, A183
- Cardiel, N., Pascual, S., Gallego, J., et al. 2019, in *Highlights on Spanish Astrophysics X, Proc. of the XIII Scientific Meeting of the Spanish Astronomical Society*, ed. B. Montesinos, A. Asensio-Ramos, F. Buitrago, R. Schödel, E. Villaver, S. Pérez-Hoyos, & I. Ordóñez-Etxeberria, 605
- Chambers, K. C., Magnier, E. A., Metcalfe, N., et al. 2019, *arXiv:1612.05560v4 [astro-ph.IM]*
- Cornachione, M. A., Morgan, C. W., Burger, H. R., et al. 2020, *ApJ*, 905, A7
- Dyrland, K. 2019, Master Thesis, University of Oslo (available at <http://urn.nb.no/URN:NBN:no-73119>)
- Eigenbrod, A., Courbin, F., Meylan, G., et al. 2008, *A&A*, 490, 933
- Fian, C., Mediavilla, E., Jiménez-Vicente, J., et al. 2021a, *A&A*, 654, A70
- Fian, C., Mediavilla, E., Motta, V., et al. 2021b, *A&A*, 653, A109
- Flewelling, H. A., Magnier, E. A., Chambers, K. C., et al. 2020, *ApJS*, 251, A7
- Garzón, F., Castro, N., Insausti, M., et al. 2016, *Proc. SPIE*, 9908, 99081J
- Gil-Merino, R., Goicoechea, L. J., Shalyapin, V. N., & Braga, V. F. 2012, *ApJ*, 744, A47
- Goicoechea, L. J., & Shalyapin, V. N. 2016, *A&A*, 596, A77
- Goicoechea, L. J., & Shalyapin, V. N. 2019, *ApJ*, 887, A126
- Goicoechea, L. J., Artamonov, B. P., Shalyapin, V. N., et al. 2020, *A&A*, 637, A89
- Gomer, M. R., & Williams, L. L. R. 2021, *MNRAS*, 504, 1340
- Holder, G. P., & Schechter, P. L. 2003, *ApJ*, 589, 688
- Howell, S. B. 2006, *Handbook of CCD Astronomy* (Cambridge Univ. Press, Cambridge)
- Jackson, N. 2015, *Living Rev. Relat.*, 18, 2
- Keeton, C. R. 2001, *arXiv:astro-ph/0102340*
- Keeton, C. R. 2004, *Software for Gravitational Lensing (gravlens 1.06 User Manual)*
- Kochanek, C. S. 2004, *ApJ*, 605, 58
- Lee, C.-H. 2017, *A&A*, 605, L8
- Lee, C.-H. 2018, *MNRAS*, 475, 3086
- Liao, K., Treu, T., Marshall, P., et al. 2015, *ApJ*, 800, A11
- Lindgren, L., Klioner, S. A., Hernández, J., et al. 2021, *A&A*, 649, A2
- Luhtaru, R., Schechter, P. L., & de Soto, K. M. 2021, *ApJ*, 915, A4
- Massey, P., & Davis, L. E. 1992, *A User’s Guide to Stellar CCD Photometry with IRAF* (Technical Report)
- McLeod, B. A., Bernstein, G. M., Rieke, M. J., & Weedman, D. W. 1998, *AJ*, 115, 1377
- Melo, A., Motta, V., Godoy, N., et al. 2021, *A&A*, 656, A108
- Millon, M., Tewes, M., Bonvin, V., et al. 2020a, *JOSS*, 5(53), 2654
- Millon, M., Courbin, F., Bonvin, V., et al. 2020b, *A&A*, 640, A105
- Morgan, C. W., Kochanek, C. S., Morgan, N. D., & Falco, E. E. 2010, *ApJ*, 712, 1129
- Morgan, C. W., Hyer, G. E., Bonvin, V., et al. 2018, *ApJ*, 869, A106
- Motta, V., Mediavilla, E., Falco, E., & Muñoz, J. A. 2012, *ApJ*, 755, A82
- Pelt, J., Kayser, R., Refsdal, S., & Schramm, T. 1996, *A&A*, 305, 97
- Poindexter S., Morgan N., & Kochanek C. S. 2008, *ApJ*, 673, 34
- Rubin, K. H. R., O’Meara, J. M., Cooksey, K. L., et al. 2018, *ApJ*, 859, A146
- Rusu, C. E., Fassnacht, C. D., Sluse, D., et al. 2017, *MNRAS*, 467, 4220
- Schmidt, R. W., & Wambsganss, J. 2010, *GRGr*, 42, 2127
- Schmidt, T., Treu, T., Birrer, S., et al. 2022, *arXiv:2206.04696v1 [astro-ph.CO]*
- Shajib, A. J., Birrer, S., Treu, T., et al. 2019, *MNRAS*, 483, 5649
- Shajib, A. J., Birrer, S., Treu, T., et al. 2021, *MNRAS*, 501, 2833
- Shakura, N. I., & Sunyaev, R. A. 1973, *A&A*, 24, 337
- Shalyapin, V. N., & Goicoechea, L. J. 2017, *ApJ*, 836, A14
- Shalyapin, V. N., Goicoechea, L. J., Morgan, C. W., et al. 2021, *A&A*, 646, A165
- Sheinis, A. I., Bolte, M., Epps, H. W., et al. 2002, *PASP*, 114, 851
- Shu, Y., Bolton, A. S., Moustakas, L. A., et al. 2016, *ApJ*, 820, A43
- Sluse, D., Claeskens, J. F., Hutsemékers, D., & Surdej, J. 2007, *A&A*, 468, 885
- Sluse, D., Chantry, V., Magain, P., Courbin, F., & Meylan, G. 2012, *A&A*, 538, A99
- Stetson, P. B. 1987, *PASP*, 99, 191
- Tewes, M., Courbin, F., & Meylan, G. 2013, *A&A*, 553, A120
- The Event Horizon Telescope Collaboration et al. 2019, *ApJL*, 875, L1
- The Event Horizon Telescope Collaboration et al. 2022, *ApJL*, 930, L12
- Tody, D. 1986, *Proc. SPIE*, 627, 733
- Tody, D. 1993, in *ASP Conf. Ser. 52, Astronomical Data Analysis Software and Systems II*, ed. R. J. Hanisch, R. J. V. Brissenden, & Jeannette Barnes (San Francisco: ASP), 173
- Treu, T., & Marshall, P. J. 2016, *A&ARv*, 24, A11
- Vestergaard, M., & Peterson, B. M. 2006, *ApJ*, 641, 689